

Quantum optimal control pathways of ozone isomerization dynamics subject to competing dissociation: A two-state one-dimensional model

Cite as: J. Chem. Phys. **140**, 084305 (2014); <https://doi.org/10.1063/1.4865813>

Submitted: 27 August 2013 . Accepted: 03 February 2014 . Published Online: 25 February 2014

Yuzuru Kurosaki, Tak-San Ho, and Herschel Rabitz



View Online



Export Citation



CrossMark

ARTICLES YOU MAY BE INTERESTED IN

The transition from the open minimum to the ring minimum on the ground state and on the lowest excited state of like symmetry in ozone: A configuration interaction study

The Journal of Chemical Physics **144**, 104304 (2016); <https://doi.org/10.1063/1.4942019>

New analytical model for the ozone electronic ground state potential surface and accurate ab initio vibrational predictions at high energy range

The Journal of Chemical Physics **139**, 134307 (2013); <https://doi.org/10.1063/1.4821638>

Quantum optimal control of isomerization dynamics of a one-dimensional reaction-path model dominated by a competing dissociation channel

The Journal of Chemical Physics **131**, 044306 (2009); <https://doi.org/10.1063/1.3185565>

PHYSICS TODAY
WHITEPAPERS

ADVANCED LIGHT CURE ADHESIVES

Take a closer look at what these environmentally friendly adhesive systems can do

READ NOW

PRESENTED BY
MASTERBOND
ADHESIVES • SEALANTS • COATINGS



Quantum optimal control pathways of ozone isomerization dynamics subject to competing dissociation: A two-state one-dimensional model

Yuzuru Kurosaki,^{1,a)} Tak-San Ho,^{2,b)} and Herschel Rabitz^{2,c)}

¹Quantum Beam Science Directorate, Tokai Research and Development Center, Japan Atomic Energy Agency, Tokai, Ibaraki 319-1195, Japan

²Department of Chemistry, Princeton University, Princeton, New Jersey 08544, USA

(Received 27 August 2013; accepted 3 February 2014; published online 25 February 2014)

We construct a two-state one-dimensional reaction-path model for ozone open \rightarrow cyclic isomerization dynamics. The model is based on the intrinsic reaction coordinate connecting the cyclic and open isomers with the $O_2 + O$ asymptote on the ground-state $^1A'$ potential energy surface obtained with the high-level *ab initio* method. Using this two-state model time-dependent wave packet optimal control simulations are carried out. Two possible pathways are identified along with their respective band-limited optimal control fields; for pathway 1 the wave packet initially associated with the open isomer is first pumped into a shallow well on the excited electronic state potential curve and then driven back to the ground electronic state to form the cyclic isomer, whereas for pathway 2 the corresponding wave packet is excited directly to the primary well of the excited state potential curve. The simulations reveal that the optimal field for pathway 1 produces a final yield of nearly 100% with substantially smaller intensity than that obtained in a previous study [Y. Kurosaki, M. Artamonov, T.-S. Ho, and H. Rabitz, *J. Chem. Phys.* **131**, 044306 (2009)] using a single-state one-dimensional model. Pathway 2, due to its strong coupling to the dissociation channel, is less effective than pathway 1. The simulations also show that nonlinear field effects due to molecular polarizability and hyperpolarizability are small for pathway 1 but could become significant for pathway 2 because much higher field intensity is involved in the latter. The results suggest that a practical control may be feasible with the aid of a few lowly excited electronic states for ozone isomerization. © 2014 AIP Publishing LLC. [<http://dx.doi.org/10.1063/1.4865813>]

I. INTRODUCTION

Quantum optimal control using ultrashort pulse lasers is receiving attention as a tool to achieve a desired dynamical objective in many research domains of physics, chemistry, and engineering. In the optimal control of chemical reaction dynamics¹⁻³ extensive studies have been made to realize chemical processes that are often inaccessible by traditional chemical means. A particularly challenging goal is to reach a target state when the reaction competes with energetically more accessible, but undesired processes. Control of ozone (O_3) isomerization from the open isomer to the cyclic (or ring) counterpart is such an example; the isomerization competes with molecular dissociation into the oxygen molecule and atom, which is energetically more favorable.

The photochemistry of ozone is of keen interest because of its crucial role in the stratosphere. In addition, the prospect that a cyclic form of ozone may exist has presented an intriguing topic for exploration. Since the first suggestion by Pauling,⁴ the cyclic ozone and its isomers in the gas phase have been the subject of numerous theoretical studies.⁵⁻³³ The cyclic form is predicted to exist at a local minimum on the ground-state potential surface, being about 0.05 a.u. higher in energy than the open one (global minimum) and about

0.04 a.u. lower than the barrier separating the two isomers. Despite the theoretical predictions, the cyclic form of ozone has thus far not been detected in the gas phase. This lack of success might be due to the competing dissociation channel, which is about 0.01 a.u. lower in energy than the cyclic form. A recent theoretical study³¹ revealed that the cyclic \rightarrow open isomerization of ozone is faster than previously believed due to strong tunneling, which might also partly explain the unsuccessful observation of the cyclic form. This result suggests that the cyclic form may need to be stabilized as a complex with other species. In this regard a computational study³⁴ based on density functional theory considered the possibility of trapping the cyclic form in transition metal complexes. As far as we know, the only experimental evidence of the cyclic form is from transmission electron diffraction data of the adsorbed molecule in an MgO (111) surface.³⁵ The present work considers only gas-phase cyclic ozone formation and explores the possibility of quantum control of the open \rightarrow cyclic isomerization process.

In a previous paper³³ we carried out optimal control calculations to obtain electric fields that can realize the open \rightarrow cyclic isomerization of ozone. Those calculations used a one-dimensional (1D) single (ground) potential model containing a dominant dissociation channel. The intensity of the resultant optimal fields was high in order to enable quick transition from the open form to the targeted cyclic counterpart and avoid undesirable leakage into the dissociation channel.

^{a)}kurosaki.yuzuru@jaea.go.jp

^{b)}tsho@Princeton.EDU

^{c)}hrabitz@Princeton.EDU

In the present work we consider a different and more realistic control scenario for ozone isomerization using an effective two-state model, constructed from five lowest-lying adiabatic $^1A'$ electronic potential energy surfaces, aiming at not only obtaining a better understanding of the underlying control dynamics but also identifying the likely control pathways with less intense optimally shaped (band-limited) laser pulses. The control pathways involve electronic excitations, nuclear vibrational transitions, and nonadiabatic processes at an avoided crossing (AC) point between the ground and excited state potential energy curves (PECs).

Although the present 1D IRC model cannot reflect all aspects of the complex wave packet dynamics of ozone isomerization in the laboratory, our main goal is to introduce a physically motivated two-state model that specifically addresses the importance of exploring particular excited electronic states in the control of ozone isomerization dynamics. In this regard our results will serve the dual purposes of (i) indicating the way ahead towards more comprehensive models as well as (ii) providing guidance to the likely general nature of control resources needed in the laboratory for ozone isomerization.

The paper is organized as follows. Section II describes the two-state 1D reaction-path model and Sec. III presents the optimal control theory (OCT) employed in this work. We consider two control pathways with differing nonadiabatic couplings and transition dipole moments, as described in Sec. IV. Section V presents the results of OCT simulations and Sec. VI provides a summary of the paper.

II. MODEL DESCRIPTION

A. *Ab initio* calculations

In the previous study³³ a single-state 1D reaction-path model was constructed based on the intrinsic reaction coordinate (IRC)³⁶ defined as the minimum energy path connecting the cyclic and open isomers with the $O_2 + O$ asymptote on the ground-state $^1A'$ potential energy surface (PES). To calculate the IRC we employed the *ab initio* data obtained by Siebert *et al.*²¹ at the MRCI+Q/cc-pVQZ level and created a PES using the reproducing kernel Hilbert space interpolation method.³⁷

In the present study the effects of electronically excited PESs on the controlled dynamics of ozone isomerization are investigated. We construct a two-state diabatic 1D reaction-path model by carrying out *ab initio* molecular orbital calculations at 211 geometries of the C_s point group along the previously determined IRC. Specifically, a two-state adiabatic 1D reaction-path model is constructed based on the lowest-five PECs along the IRC. Moreover, to facilitate the optimal control simulations, a two-state diabatic 1D reaction path model is built via the two-state diabaticization procedure described below.

The *ab initio* calculations used the MOLPRO program.³⁸ We first performed state-averaged complete-active-space self-consistent field (SA-CASSCF) computations to obtain five $^1A'$ state PECs. The active space consists of the $2p$ orbitals of oxygen, occupied by 12 electrons, which is referred to

as CASSCF(12,9). The $1s$ and $2s$ orbitals are doubly occupied but fully optimized in the CASSCF procedure. To consider dynamical correlation effects we carried out internally contracted multi-reference configuration interaction (icMRCI) calculations^{39,40} with single and double excitations (icMRSDCI) for each electronic state obtained with the CASSCF(12,9) method. In the reference configurations of the icMRSDCI calculations the $2p$ orbitals are singly or doubly occupied and correlated through single and double excitations, the $2s$ orbitals are doubly occupied and correlated, and the $1s$ orbitals are doubly occupied and not correlated. The aug-cc-pVTZ⁴¹ basis set is used in all calculations.

B. Diabatization

This subsection provides the diabaticization procedures⁴² for the PECs, dipole moments (DMs), and transition dipole moments (TDMs). The general relationship between the adiabatic (superscript a) and diabatic (superscript d) representations for two electronic states is given by

$$\begin{pmatrix} \phi_1^d \\ \phi_2^d \end{pmatrix} = \begin{pmatrix} \cos \theta & -\sin \theta \\ \sin \theta & \cos \theta \end{pmatrix} \begin{pmatrix} \phi_1^a \\ \phi_2^a \end{pmatrix}, \quad (1)$$

where θ is the mixing angle. Thus, the diagonal elements of the diabatic potential matrix are

$$V_{11}^d = V_{11}^a \cos^2 \theta + V_{22}^a \sin^2 \theta, \quad (2)$$

$$V_{22}^d = V_{11}^a \sin^2 \theta + V_{22}^a \cos^2 \theta, \quad (3)$$

and the off-diagonal elements determining the magnitude of the diabatic coupling are

$$V_{12}^d = V_{21}^d = (V_{11}^a - V_{22}^a) \sin \theta \cos \theta. \quad (4)$$

The mixing angle is in the interval $0 \leq \theta \leq \pi/2$, and when $\theta = 0$ or $\pi/2$ the diabatic and adiabatic states are identical with the off-diagonal elements having the value $V_{12}^d = V_{21}^d = 0$. When $\theta = \pi/4$, the factor $\sin \theta \cos \theta$ in Eq. (4) has the maximum value of $1/2$ and the off-diagonal elements have the largest magnitude, $V_{12}^d = V_{21}^d = (V_{11}^a - V_{22}^a)/2$, which occurs at AC points. Defining ΔE_x as the difference in energy between the two adiabatic PECs at an AC point, then $V_{12}^d = \Delta E_x/2$ at this point. Ideally, the mixing angle θ around the crossing point should be determined with suitable quantum mechanical techniques; for our two-state model, the coordinate-dependent off-diagonal element $V_{12}^d(s)$ was fitted to a Gaussian form:

$$V_{12}^d(s) = \frac{\Delta E_x}{2} \exp(-\delta(s - s_x)^2), \quad (5)$$

where s denotes the IRC, $s_x = 5.81$ a.u. is the AC point, and $\delta = \ln 10 \times 300 \approx 691$. The IRC has the units of $\text{amu}^{1/2}$ bohr, but in what follows the units for s are written as a.u. (atomic unit) for brevity. The parameter δ was determined by the relation

$$V_{12}^d(s_x \pm s_d) = A V_{12}^d(s_x), \quad (6)$$

where the range is $s_d = 0.1$ a.u. and the coupling amplitude is $A = 10^{-3}$.

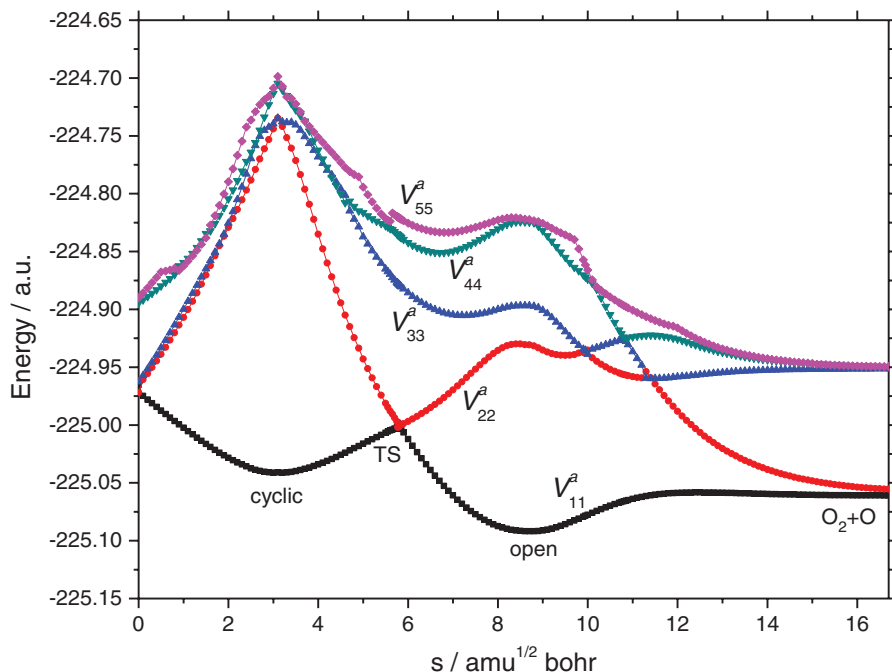


FIG. 1. The five lowest-lying adiabatic $^1A'$ PECs along the IRC (s) obtained at the icMRSDCI/aug-cc-pVTZ level of theory.

The dipole moments represented with the diabatic basis at geometries along the IRC can be obtained from the DMs and TDMs in the adiabatic representation calculated at the same level of theory as the PECs. The two-state adiabatic-diabatic transformations for DMs and TDMs are given by

$$\mu_{11}^d = \mu_{11}^a \cos^2 \theta - 2\mu_{12}^a \sin \theta \cos \theta + \mu_{22}^a \sin^2 \theta, \quad (7)$$

$$\mu_{22}^d = \mu_{11}^a \sin^2 \theta + 2\mu_{12}^a \sin \theta \cos \theta + \mu_{22}^a \cos^2 \theta, \quad (8)$$

$$\begin{aligned} \mu_{12}^d = \mu_{21}^d = & \mu_{11}^a \sin \theta \cos \theta \\ & + \mu_{12}^a (\cos^2 \theta - \sin^2 \theta) - \mu_{22}^a \sin \theta \cos \theta. \end{aligned} \quad (9)$$

The mixing angle θ at s on the IRC is determined from $V_{12}^d(s)$ and Eq. (4). We use these diabatic DMs and TDMs, i.e., μ_{11}^d , μ_{22}^d , and μ_{12}^d , in the optimal control calculations described below. Equations (7)–(9) can also be applied to the transformations of the matrix elements for the polarizability and hyperpolarizability.

C. PECs, DMs, and eigenfunctions

Figure 1 shows the five lowest-lying adiabatic $^1A'$ PECs along the IRC (s) obtained at the icMRSDCI/aug-cc-pVTZ level of theory. Figure 2(a) presents the two-state diabatic potential model used in the optimal control calculations, constructed from those five lowest-lying adiabatic $^1A'$ PECs given in Fig. 1. The details of constructing the diabatic two-state potential model are explained in the supplementary material.⁴³ As shown in Fig. 1, in general many open-cyclic isomerization pathways are possible due to the appearance of many closely coupled excited PECs; however, by using particular band-limited electric fields (obtained here with frequency

bandpass filters, as explained in Sec. III A), the isomerization pathways may be considerably simplified, resulting in the two-state model in Fig. 2. The model starts with the molecule in the open isomer configuration, followed by passage through the AC point, and finally reaching the cyclic configuration. The proposed two-state model is based on the facts that: (i) The higher excited states can be made energetically inaccessible with laser fields of moderate intensity and of suitably chosen bandwidths. (ii) The diabatic couplings are small due to small energy gaps at the crossing points (~ 0.002 hartree at $s = 10.0$ a.u. between V_{22}^a and V_{33}^a ; ~ 0.001 hartree at $s = 10.8$ a.u. between V_{33}^a and V_{44}^a ; < 0.001 hartree at $s = 11.4$ a.u. between V_{22}^a and V_{33}^a). Thus, the diabatic couplings only play a very small role when compared with the interaction between ozone and the laser fields in the corresponding controlled dynamics. (iii) The Franck-Condon factor between V_{11}^a and V_{22}^a is much larger than those between V_{11}^a and all other excited states, as shown in Fig. 1.

As shown in Fig. 2(a), the two-state model contains two main minima, an AC point, and a shallow secondary minimum. The first main minimum (the open isomer of ozone) is located at $s = 8.7$ a.u. on the diabatic PEC V_{11}^d , while the second main minimum (the cyclic isomer of ozone) is located at $s = 3.1$ a.u. on V_{22}^d . The crossing point (the transition state separating the two isomers) is located at $s = 5.8$ a.u. The shallow secondary well (on the diabatic PEC V_{22}^d) is located at $s = 9.5$ a.u. and supports a few bound levels. The inset in the figure shows the diabatic coupling V_{12}^d as a function of s , which is responsible for the field-free nonadiabatic process. In addition, Fig. 3 depicts the z components of the dipole moment matrix elements $\mu_{11}^d(s)$, $\mu_{22}^d(s)$, and $\mu_{12}^d(s)$ in the diabatic basis, constructed from the corresponding adiabatic ones, along the IRC s . The z axis is placed along the bisector of the apex angle of the open isomer of ozone. Beyond

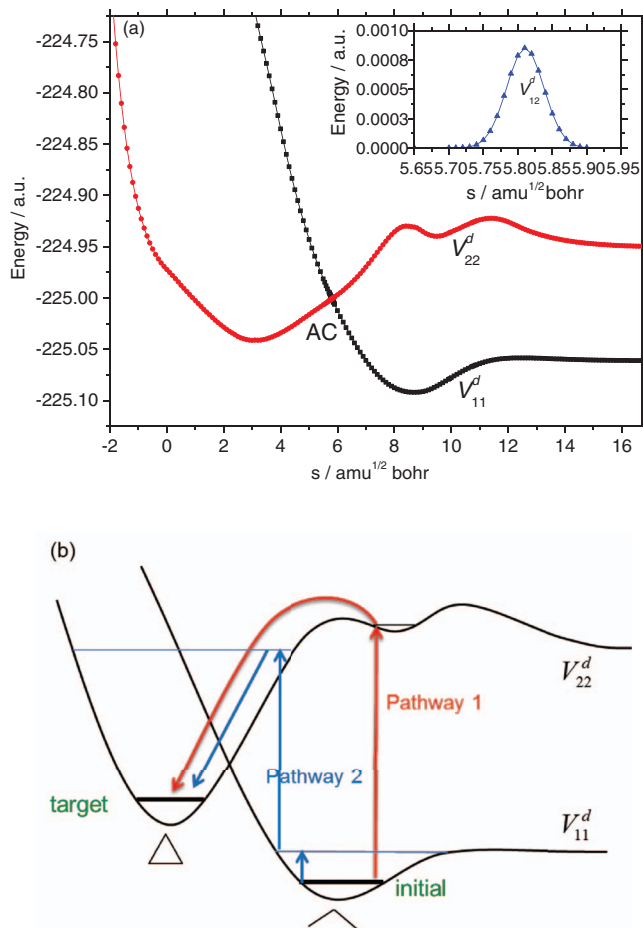


FIG. 2. (a) The two-state model consisting of two diabatic PECs V_{11}^d and V_{22}^d and the diabatic coupling V_{12}^d (inset). (b) Control pathways 1 (red) and 2 (blue).

the DMs and TDM, nonlinear field effects due to the molecular polarizability and hyperpolarizability could become important in the presence of intense fields. Subsection II D will discuss the nonlinear effects. The supplementary material⁴³ presents the details of constructing the diabatic dipole model.

The eigenvalues and eigenfunctions for V_{11}^d and V_{22}^d are calculated, respectively, using the Fourier grid Hamiltonian method⁴⁴ with 512 evenly spaced grid points on the IRC from $s = -2.0$ to 16.7 a.u. Table S5 in the supplementary material⁴³ shows the lowest ten eigenvalues, obtained by separately diagonalizing the $n \times n$ V_{11}^d and V_{22}^d blocks, with the grids of 128, 256, and 512 points. The results are well converged with 512 grid points.

D. Nonlinear field effects

The components of the induced dipole moment μ due to the presence of an electric field $\epsilon(t)$ can be written (using the convention of summation over repeated indices) as

$$\mu_i = \mu_i^0 + (2!)^{-1} \alpha_{ij} \epsilon_j + (3!)^{-1} \beta_{ijk} \epsilon_j \epsilon_k + \dots, \quad (10)$$

$i, j, k = x, y, z,$

where μ_i^0 , α_{ij} , and β_{ijk} are the components of the permanent dipole moment, polarizability tensor, and hyperpolariz-

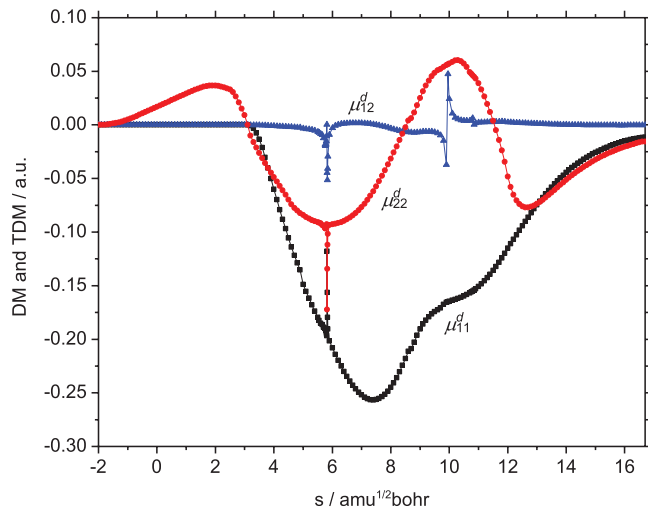


FIG. 3. The matrix elements on the diabatic basis for the z components of the permanent dipole moment as a function of the IRC s . The z axis lies along the bisector of the apex angle of the open isomer of ozone.

ability tensor, respectively. Thus, the interaction potential V_{int} between the dipole and the electric field is given by

$$V_{int} = -\boldsymbol{\mu} \cdot \boldsymbol{\epsilon} = -(\mu_i^0 \epsilon_i + (2!)^{-1} \alpha_{ij} \epsilon_i \epsilon_j + (3!)^{-1} \beta_{ijk} \epsilon_i \epsilon_j \epsilon_k + \dots), \quad i, j, k = x, y, z. \quad (11)$$

Here we consider the electric field linearly polarized along the z axis (i.e., $\epsilon_x = \epsilon_y = 0$) such that Eq. (11) reduces to

$$V_{int} = -(\mu_z^0 \epsilon_z + (2!)^{-1} \alpha_{zz} \epsilon_z^2 + (3!)^{-1} \beta_{zzz} \epsilon_z^3 + \dots). \quad (12)$$

In what follows we omit the super and subscripts for ϵ_z , μ_z^0 , α_{zz} , and β_{zzz} and just denote them as ϵ , μ , α , and β , respectively, for simplicity. In the simulations we first investigate the cases without the nonlinear effects, i.e., $V_{int} = -\mu\epsilon$, and then those with the nonlinear effects, i.e., $V_{int} = -(\mu\epsilon + (2!)^{-1} \alpha\epsilon^2 + (3!)^{-1} \beta\epsilon^3)$.

The z components of the matrix elements of α and β in the diabatic basis, obtained in the *ab initio* calculations, are depicted in Fig. 4. The magnitudes of α_{11}^d and α_{22}^d (10–12 a.u., Fig. 4(a)) and those of β_{11}^d and β_{22}^d (30–75 a.u., Fig. 4(b)) are much larger than that of the permanent dipole moment μ (Fig. 3). Details for constructing the diabatic two-state α and β models are given in the supplementary material.⁴³

III. OPTIMAL CONTROL SIMULATION METHOD

A. Optimal control theory

Optimal control theory (OCT)^{45–47} provides an efficient means to find an electric field that steers the wave function from an initial state as close as possible to a target counterpart. The goal is to find a control field that maximizes the transition probability of reaching the target state while also minimizing

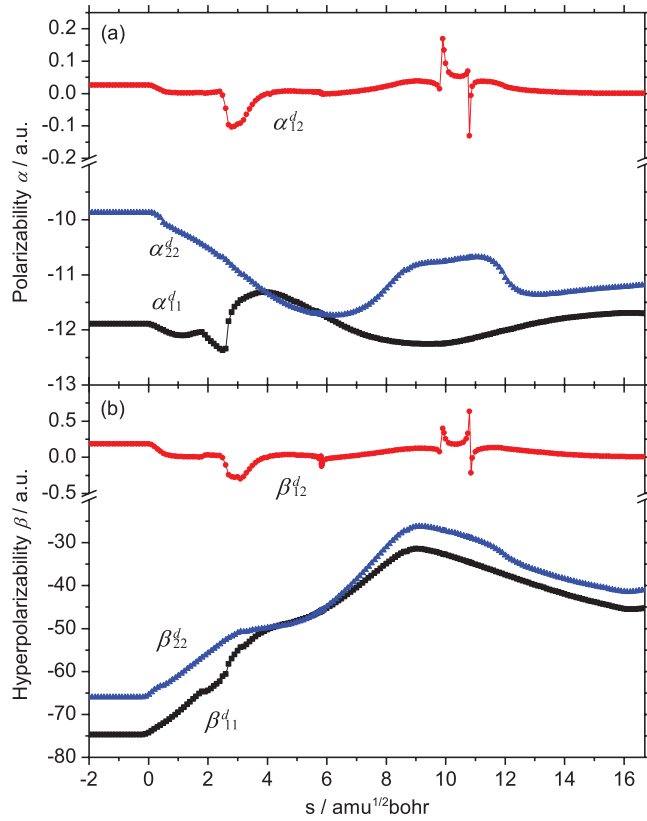


FIG. 4. The matrix elements in the diabatic basis of the z components of (a) polarizability α and (b) hyperpolarizability β as functions of the IRC s .

the laser pulse fluence, expressed by the objective functional

$$J = |\langle \psi_f | \psi(T) \rangle|^2 - \alpha_0 \int_0^T dt \varepsilon(t)^2 - 2\text{Re} \left[\langle \psi(T) | \psi_f \rangle \int_0^T dt \langle \chi(t) | \frac{\partial}{\partial t} + i(H_0 + V_{\text{int}}) | \psi(t) \rangle \right]. \quad (13)$$

The first term is the transition probability to be maximized, where $|\psi(t)\rangle$ is the system state propagated from time $t = 0$ to T and $|\psi_f\rangle$ is the target state. The second term is the laser fluence to be minimized, where α_0 is a positive constant. The third term is the dynamical constraint, where $\chi(t)$ is the Lagrange multiplier, Re denotes the real part of a complex number, H_0 is the field-free Hamiltonian, and V_{int} is the interaction potential in Eq. (12). The following coupled equations

$$i \frac{\partial \psi(t)}{\partial t} = (H_0 + V_{\text{int}}(t))\psi(t), \quad \psi(0) = \psi_0, \quad (14a)$$

$$i \frac{\partial \chi(t)}{\partial t} = (H_0 + V_{\text{int}}(t))\chi(t), \quad \chi(T) = \psi_f, \quad (14b)$$

and

$$\alpha_0 \varepsilon(t) = -\text{Im}[\langle \psi(T) | \psi_f \rangle \langle \chi(t) | - V_{\text{int}}/\varepsilon(t) | \psi(t) \rangle], \quad (14c)$$

are the necessary optimality conditions for $\delta J = 0$ with respect to $\psi(t)$, $\chi(t)$, and $\varepsilon(t)$, with Im denoting the imaginary part. Equations (14a)–(14c) are solved iteratively with the aid

of the conjugate gradient method described in Ref. 32. In each iteration, the control electric field $\varepsilon(t)$ is filtered within a prescribed bandwidth using the relation:

$$\bar{\varepsilon}(t) = F^{-1}[F[\varepsilon(t)]h(\omega)], \quad (15)$$

where F and F^{-1} represent Fourier and inverse Fourier transforms, respectively, and $h(\omega)$ is a filter function. In the present study, a Butterworth bandpass filter⁴⁸ is employed, i.e.,

$$h(\omega) = \left(\left[1 + \left(\frac{\omega_l}{\omega} \right)^{2n} \right] \left[1 + \left(\frac{\omega}{\omega_h} \right)^{2n} \right] \right)^{-1/2}, \quad (16)$$

where ω_l and ω_h are low and high cutoff frequencies, respectively, and n (the order of the filter) is set to 20.

B. Kinetic energy in the Hamiltonian

We need to specify the kinetic energy in the field-free Hamiltonian in terms of the IRC. Denoting the Cartesian coordinates of the i th atom as x_i , y_i , and z_i , the classical nuclear kinetic energy of an N -atom system is

$$K = \frac{1}{2} \sum_i^N m_i (\dot{x}_i^2 + \dot{y}_i^2 + \dot{z}_i^2), \quad (17)$$

where m_i is the mass of the i th nucleus and the dot stands for time derivative. The mass-scaled Cartesian coordinates are defined by

$$q_{3i-2} = \sqrt{\frac{m_i}{m_{sc}}} x_i, \quad q_{3i-1} = \sqrt{\frac{m_i}{m_{sc}}} y_i, \\ q_{3i} = \sqrt{\frac{m_i}{m_{sc}}} z_i, \quad i = 1, 2, \dots, N, \quad (18)$$

with m_{sc} being the scaling mass. Then K has the form⁴⁹

$$K = \frac{1}{2} m_{sc} \sum_i^{3N} \dot{q}_i^2. \quad (19)$$

In this coordinate system the distance has the unit of (the ratio of m_i to m_{sc})^{1/2} \times length. Considering the motion along the IRC, we have the relation between the arc length s and the mass-scaled Cartesian coordinates,

$$ds^2 = \sum_i^{3N} dq_i^2, \quad (20)$$

and the kinetic energy in terms of s can be expressed as

$$K = \frac{1}{2} m_{sc} \dot{s}^2 = \frac{1}{2m_{sc}} p_s^2, \quad (21)$$

where p_s is the momentum conjugate to s . The quantum-mechanical form of K along the IRC is obtained with the replacement $p_s = -i(\partial/\partial s)$, i.e.,

$$K = -\frac{1}{2m_{sc}} \frac{\partial^2}{\partial s^2}. \quad (22)$$

We set $m_{sc} = 1$ amu and thus the IRC has the units of amu^{1/2} \times length (in bohr).

C. Wave packet propagation

Since the controlled dynamics occur on two diabatic PECs, the Schrödinger equation can be written in matrix form:

$$i \frac{\partial}{\partial t} \boldsymbol{\psi} = \mathbf{H} \boldsymbol{\psi}, \quad (23)$$

where

$$\boldsymbol{\psi} = \begin{pmatrix} \psi_1(t) \\ \psi_2(t) \end{pmatrix}, \quad (24)$$

with $\psi_1(t)$ and $\psi_2(t)$ being the projections of the system wave packet on the diabatic PECs V_{11}^d and V_{22}^d , respectively. The Hamiltonian matrix becomes

$$\begin{aligned} \mathbf{H} &= \mathbf{T} + \mathbf{V} \\ &= \begin{pmatrix} T_1 & 0 \\ 0 & T_2 \end{pmatrix} + \begin{pmatrix} V_{11} & V_{12} \\ V_{21} & V_{22} \end{pmatrix} \\ &= \begin{pmatrix} T_1 & 0 \\ 0 & T_2 \end{pmatrix} + \begin{pmatrix} V_{11}^d - \mu_{11}^d \varepsilon(t) & V_{12}^d - \mu_{12}^d \varepsilon(t) \\ V_{21}^d - \mu_{21}^d \varepsilon(t) & V_{22}^d - \mu_{22}^d \varepsilon(t) \end{pmatrix}, \end{aligned} \quad (25)$$

where T_1 and T_2 are the kinetic-energy operators for nuclear motion on V_{11}^d and V_{22}^d , respectively. The off-diagonal elements of the potential matrix \mathbf{V} are responsible for the transitions between the two diabatic PECs due to the diabatic couplings V_{12}^d and V_{21}^d and the transition dipole moments μ_{12}^d and μ_{21}^d . Equation (23) is numerically solved using the split-operator method,^{50,51}

$$\begin{aligned} \boldsymbol{\psi}(t + \Delta t) &= \exp(-i\mathbf{V}\Delta t/2) \exp(-i\mathbf{T}\Delta t) \\ &\quad \times \exp(-i\mathbf{V}\Delta t/2) \boldsymbol{\psi}(t) + O(\Delta t^3). \end{aligned} \quad (26)$$

The fast-Fourier-transform algorithm is used to efficiently implement Eq. (26) in standard fashion. Furthermore, based on procedures proposed by Broeckhove *et al.*,^{52,53} the potential-energy matrix may be written in terms of the Pauli matrices $\boldsymbol{\sigma}_i$, as

$$\mathbf{V} = \sum_{i=0}^3 v_i \boldsymbol{\sigma}_i, \quad (27)$$

where

$$v_0 = \frac{V_{11}^d + V_{22}^d}{2}, \quad v_1 = V_{12}^d, \quad v_2 = 0, \quad v_3 = \frac{V_{11}^d - V_{22}^d}{2}, \quad (28)$$

and the exponential of the potential-energy matrix is evaluated as

$$\begin{aligned} &\exp(-i\mathbf{V}\Delta t/2) \\ &= \exp(-i v_0 \Delta t/2) \\ &\quad \times \left(\boldsymbol{\sigma}_0 \cos(|v| \Delta t/2) - i \frac{\sin(|v| \Delta t/2)}{|v|} \sum_{i=1}^3 v_i \boldsymbol{\sigma}_i \right), \end{aligned} \quad (29)$$

where

$$|v| = \left(\sum_{i=1}^3 v_i^2 \right)^{1/2}. \quad (30)$$

In the present calculation, the initial condition ψ_0 for the Schrödinger equation (14a) is the vibrational ground state of the diabatic PEC V_{11}^d , i.e., $\psi_0 = (\phi_1^1, 0)^T$ and the target state is the vibrational ground state of the diabatic PEC V_{22}^d , i.e., $\psi_f = (0, \phi_1^2)^T$ with ϕ_i^j being the i th eigenfunction for PEC V_{jj}^d . The system wave packet $\psi(t)$ is started from ψ_0 and propagated forward in time according to Eq. (14a) and, conversely, the Lagrange multiplier $\chi(t)$ is started from the target state ψ_f and propagated backward in time according to Eq. (14b). The molecular rotational motion is frozen in the wave packet propagation. The total propagation time T (i.e., the pulse length) is set to 80 000 a.u. (1.936 ps), and the number of time steps is 8192 ($= 2^{13}$). In the wave packet propagation, a damping function⁵⁴

$$f(s_i) = \sin \left[\frac{\pi}{2} \frac{(s_{\text{mask}} + \Delta s_{\text{mask}} - s_i)}{\Delta s_{\text{mask}}} \right], \quad s_i \geq s_{\text{mask}}, \quad (31)$$

is adopted to eliminate the unwanted reflection of the wave function at the grid edge, where s_{mask} is the point at which the damping function is initiated and $\Delta s_{\text{mask}} = s_{\text{max}} - s_{\text{mask}}$ is the region where the function decays from 1 to 0, with s_{max} being the maximum point of the grid. The damping function is operative only over the last 10 grid points from the edge s_{max} .

IV. IDENTIFICATION OF OPTIMAL CONTROL PATHWAYS

We have conducted optimal control simulations of the open \rightarrow cyclic isomerization of ozone and two different control pathways were identified, as schematically illustrated in Fig. 2(b), along with their respective band-limited control fields. Pathway 1 (in red) contains two steps: the wave packet for the open isomer (the ground vibrational state of V_{11}^d) is first excited electronically into the secondary well (at $s = 9.5$ a.u.) and then driven down the slope of the PEC, passing through the AC point to form the cyclic isomer (the ground vibrational state of V_{22}^d). Pathway 2 (in blue) contains three steps: the initial ground-state open isomer wave packet is first excited to high-lying vibrational levels just below the dissociation asymptote of PEC V_{11}^d , then makes a transition to vibrational levels above the AC point in the main well of PEC V_{22}^d , and finally is driven across the AC point to reach the ground vibrational state of V_{22}^d .

To obtain an initial control field for pathway 1 the total time was divided into two segments of duration, 20 000 and 60 000 a.u., for pre-optimization. In the first period an optimal field is constructed to excite the ground-state open-isomer wave packet to the shallow well of PEC V_{22}^d , and in the second period a field is optimized to drive the electronically excited molecule from the shallow well to the cyclic-isomer ground state below the AC point. These two fields are then combined into a single control field that is further optimized over the total time interval of 80 000 a.u. to attain the ultimate

open \rightarrow cyclic isomerization. Likewise for pathway 2, the total time is divided into three segments of duration, 20 000, 20 000, and 40 000 a.u., for pre-optimization. An optimal control field is constructed in each period, first for vibrational excitation of the initial wave packet in the well of PEC V_{11}^d , then for electronic excitation from the highest vibrational level in PEC V_{11}^d to a state that is only slightly above the AC point, and finally for formation of the target from the state above the AC point. Similar to pathway 1, the control fields for these three periods are combined for further optimization. The bandwidth of the control fields was constrained using the filter function given in Eq. (16) with the cutoff frequencies $\omega_l = 0.0001$ a.u. and $\omega_h = 0.3$ a.u. for pathway 1 and with the cutoff frequencies $\omega_l = 0.0001$ a.u. and $\omega_h = 0.1$ a.u. for pathway 2. These frequency windows serve to distinguish the two pathways. Specifically, for pathway 2 frequencies larger than 0.1 a.u. were removed during the field optimization such that the corresponding OCT procedure would not allow for a direct excitation of the ozone molecule from the lowest vibrational level in PEC V_{11}^d vertically into the secondary well of PEC V_{22}^d , which requires a photon of frequency of around 0.15 a.u.

In order to examine the two identified control pathways, three additional OCT calculations were carried out using different magnitudes for the diabatic couplings and TDMs: (a) the diabatic coupling is chosen to be five times larger than the *ab initio* raw data (strong diabatic coupling, red curve in Fig. 5(a)) and/or (b) the TDM based on the adiabatic representation around the AC point ($s = 5.81$ a.u.) is set to zero

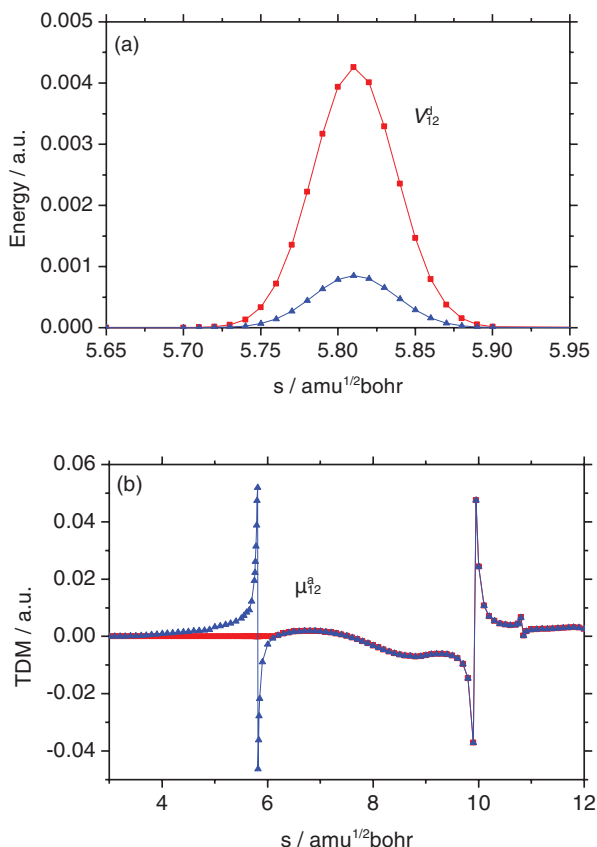


FIG. 5. Modified (a) diabatic potential (in red) and (b) adiabatic TDM (in red) used in the OCT calculations. The *ab initio* results are shown in blue.

TABLE I. Four cases of variation investigated.

	Case 1	Case 2	Case 3	Case 4
Diabatic coupling	Raw ^a	Strong ^b	Raw	Strong
TDM around the AC point	Raw	Raw	No ^c	No

^aRaw data refer to using *ab initio* calculations in the present work.

^bThe diabatic couplings are set to five times of the raw *ab initio* data.

^cThe TDMs are set to zero.

(no transition moment, red curve in Fig. 5(b)). Table I summarizes four cases applied to control along pathways 1 and 2. For comparison, the calculated diabatic coupling and TDM are shown in blue in Figs. 5(a) and 5(b), respectively. The simulations neglecting the nonlinear field effects are carried out for cases 1–4 of pathways 1 and 2, while the simulations including the nonlinear effects are performed only for case 1 of both pathways. Moreover, to examine the role of the AC point, we also checked how the amplitude A (or the width parameter) in Eqs. (5) and (6) affects the optimal control calculations by changing its value from 10^{-4} to 10^{-2} . As a result, difference between the final yields calculated for case 1 of pathway 1 with the same optimal field for $A = 10^{-3}$ was found to be less than 0.001.

In addition, we checked how the position of the grid boundary affects the results by increasing the grid edge from $s = 16.7$ a.u. to 20.0 a.u. without varying the number of grid points, 512. Using the same optimal field obtained with the grid edge at $s = 16.7$ a.u. for case 1 of pathway 1, the final yield calculated with the grid edge at $s = 20.0$ a.u. was only 0.003 smaller.

Finally, we performed *post facto* calculations to check whether the roles played by the diabatic couplings at the AC points are negligible. Specifically, using the same optimal fields obtained from the proposed two-state model (with the diabatic coupling included), we carried out the underlying isomerization dynamics *post facto* for case 1 of pathways 1 and 2 with no diabatic coupling. As a result, we found that the final yields were only 0.001 and 0.002 smaller than the yields, 0.973 and 0.637 (Table II), obtained with the diabatic coupling between V_{11}^d and V_{22}^d , respectively, for pathways 1 and 2, indicating that the diabatic coupling around the AC point at $s = 5.8$ a.u. is small and hardly affects the control dynamics. Since the energy gap at $s = 5.8$ a.u. between V_{11}^d and V_{22}^d , 0.00170 hartree, is comparable with or slightly larger than the energy gaps at other AC points (see Sec. II C), this result strongly suggests that the corresponding wave packet is likely to pass through all AC points diabatically, i.e., the chances of all other excited diabatic states, other than V_{22}^d , participating in the controlled dynamics are very low as long as the corresponding optimal control fields are properly bandlimited in their frequencies.

V. RESULTS AND DISCUSSION

A. Pathway 1

1. Case 1

Figure 6 shows (a) the optimized field and (b) its power spectrum from the OCT calculation without the nonlinear

TABLE II. Simulation results.

Pathway	α_0^a	Max. field amp. (a.u.)	Fluence (a.u.)	Yield
No nonlinear field effects ^b				
Pathway 1				
Case 1	0.0005	0.222	140.4	0.973
Case 2	0.0005	0.253	138.1	0.946
Case 3	0.0005	0.237	133.6	0.985
Case 4	0.0005	0.242	134.7	0.946
Pathway 2				
Case 1	0.0001	0.774	1318.6	0.637
Case 2	0.0001	0.774	1317.8	0.531
Case 3	0.0001	0.774	1318.6	0.657
Case 4	0.0001	0.774	1318.4	0.540
Nonlinear field effects ^c				
Pathway 1				
Case 1	0.0005	0.190	134.3	0.975
Pathway 2				
Case 1	0.00001	0.855	607.1	0.858

^aWeight in the cost function of Eq. (13).

^b $V_{int} = -\mu\varepsilon$ is adopted.

^c $V_{int} = -(\mu\varepsilon + (2!)^{-1}\alpha\varepsilon^2 + (3!)^{-1}\beta\varepsilon^3)$ is adopted.

field effects for case 1 of pathway 1. The optimized field, Fig. 6(a), is highly oscillatory for $t < 20\,000$ a.u. and becomes considerably less so for $t > 40\,000$ a.u. The power spectrum, Fig. 6(b), contains a strong high frequency component corresponding to the electronic excitation energy for the

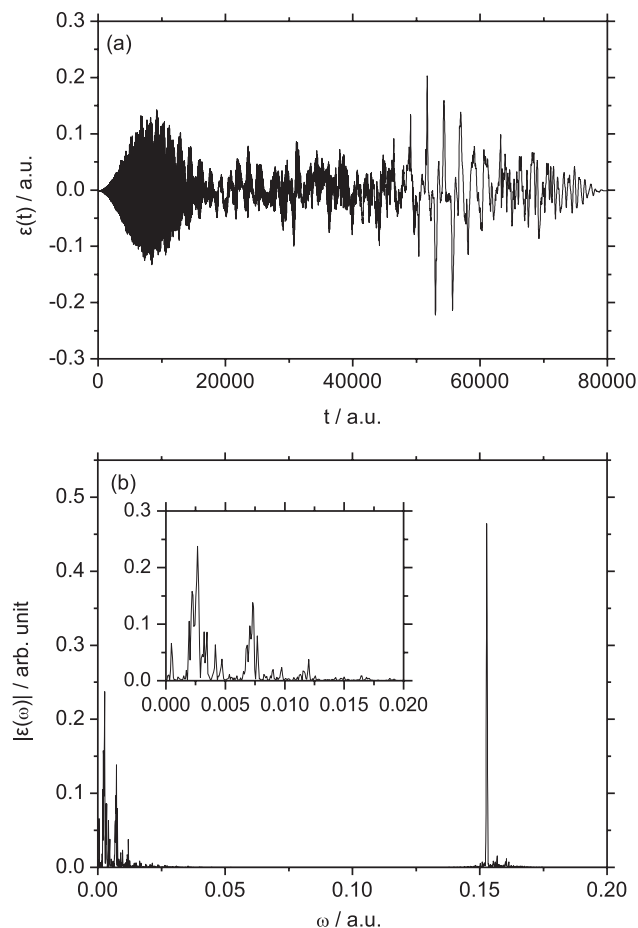


FIG. 6. (a) The optimal field and (b) its spectrum for case 1 of pathway 1, obtained without nonlinear field effects.

transition from the initial state to the secondary well of PEC V_{22}^d . The power spectrum also contains modest low frequency components, including some overtones (see the inset), corresponding to the vibrational level spacings of diabatic PEC V_{22}^d . Table II summarizes the results for all of the cases. The optimal field (maximum amplitude 0.222 a.u. and fluence 140.4 a.u.) for case 1 of pathway 1 produces a final yield of 0.973.

Figure 7 shows the temporal evolution of (a) the expectation value of the molecular field-free Hamiltonian, $\langle H_0 \rangle$, (b) the expectation value of position, $\langle s \rangle$, and (c) the populations $\langle \psi_1 | \psi_1 \rangle$ and $\langle \psi_2 | \psi_2 \rangle$ in the diabatic states V_{11}^d and V_{22}^d , respectively, and the norm $\langle \psi | \psi \rangle$ of the total wave packet. These plots reveal different aspects of the transition dynamics associated with the optimal control field given in Fig. 6(a). Figure 7(a) shows that direct electronic transitions take place between $t = 0$ and 40 000 a.u., characterized by large oscillations in $\langle H_0 \rangle$. Figure 7(b) reveals that $\langle s \rangle$ oscillates with small amplitude around $s = 9.5$ a.u. (see Fig. 2(a)) between $t = 10\,000$ and 30 000 a.u., indicating that a vertical electronic transition takes place between the open isomer and the shallow secondary well of PEC V_{22}^d . This is followed by oscillations of much larger amplitude between $t = 35\,000$ and 70 000 a.u., before finally reaching the target equilibrium position at $t = 80\,000$ a.u., indicating that the descending transitions take place over a ladder of vibrational levels of PEC V_{22}^d . Figure 7(c) depicts the individual temporal populations on the two diabatic PECs, respectively, consistent with the findings

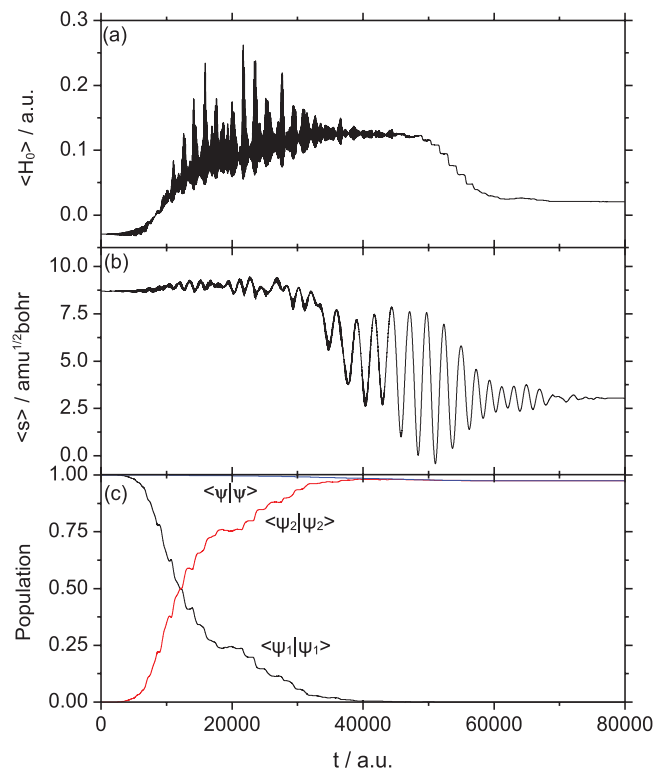


FIG. 7. Temporal evolution driven by the optimal field for case 1 of pathway 1 given in Fig. 6(a), obtained without nonlinear field effects: (a) the expectation value of molecular field-free Hamiltonian, $\langle H_0 \rangle$. The origin of the vertical axis corresponds to the asymptotic energy of V_{11}^d ; (b) the expectation value of position, $\langle s \rangle$; (c) the populations of the diabatic states V_{11}^d and V_{22}^d and the norm of wave packets, $\langle \psi_1 | \psi_1 \rangle$, $\langle \psi_2 | \psi_2 \rangle$, and $\langle \psi | \psi \rangle$.

in Figs. 7(a) and 7(b). There is a small total population loss due to the dissociation process. Snapshots of the wave-packet components for PECs V_{11}^d and V_{22}^d are shown in Fig. S3 in the supplementary material,⁴³ explaining the temporal changes observed in Fig. 7.

2. Cases 2–4

Final optimal yields for cases 2–4 of pathway 1 are between 0.95 and 0.99 and the corresponding optimal control fields have amplitudes between 0.24 and 0.25 a.u. and fluences between 134 and 138 a.u. These values are close to those obtained for case 1 (Table II). Furthermore, the optimal fields, the power spectra, $\langle H_0 \rangle$, $\langle s \rangle$, state populations, and wave-packet propagation for cases 2–4 all have similar behavior to those for case 1 (not shown). These findings may be attributed to the fact that the secondary shallow well on PEC V_{22}^d lies sufficiently high above the AC point so that the emerging wave packet has enough energy to hop over the AC point very quickly. It is likely, however, that a much stronger diabatic coupling than five times the *ab initio* raw data would substantially lower the final yield. Nonlinear field effects on the control results for pathway 1 are small, as shown in Table II, because the fields are only of moderate intensity.

B. Pathway 2

1. Case 1

The OCT results for case 1 of pathway 2, excluding nonlinear field effects, are plotted in Figs. 8 and 9. Figure 8 shows: (a) the temporal field profile and (b) its power spectrum. Of particular note in Fig. 8(a) is the large spikes between $t = 20\,000$ and $50\,000$ a.u. These spikes are responsible for the electronic transition to PEC V_{22}^d of the residual wave packet moving back and forth in the well of PEC V_{11}^d and repeatedly passing through a position appropriate for the electronic transitions. It is found in Fig. 8(b) that the optimal control field contains several very strong, high frequency components near the upper limit (0.1 a.u.) within a small frequency window. These high frequencies are responsible for the electronic excitation from V_{11}^d to V_{22}^d . The spectrum also contains much weaker components in the low frequency region, which produces vibrational transitions in V_{11}^d and V_{22}^d . A Husimi plot giving time-frequency correlation of the optimal field is shown in Fig. S6 in the supplementary material.⁴³ Table II shows that a final yield of 0.637 is obtained along with the maximum field amplitude and fluence equal to 0.774 and 1318.6 a.u., respectively. Despite the high control field intensity and fluence involved, the final yield for case 1 of pathway 2 is much smaller than that for the same case of pathway 1. This happens because pathway 1 involves a direct electronic transition between the ground vibrational state of PEC V_{11}^d and the shallow well of PEC V_{22}^d , whereas pathway 2 involves intermediate transitions to some high vibrational levels close to the V_{11}^d dissociation limit, thus, incurring loss to dissociation. This result suggests that a very intense, short control pulse would be required with pathway 2 in order to quickly pump the molecule into PEC V_{22}^d and thereby minimize the loss.

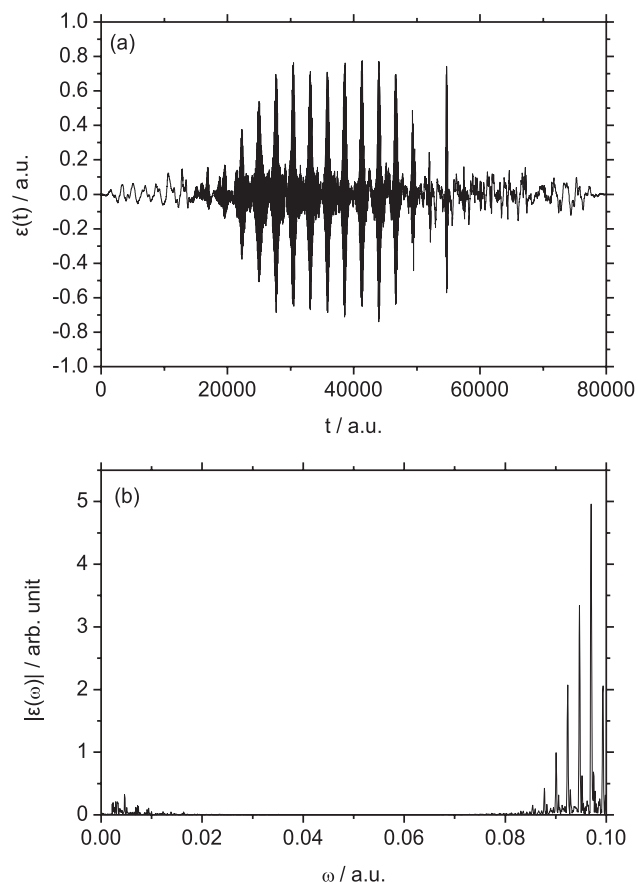


FIG. 8. (a) The optimal field and (b) its spectrum for case 1 of pathway 2, obtained without nonlinear field effects.

Figure 9(a) displays the expectation value of field-free molecular Hamiltonian $\langle H_0 \rangle$ as a function of time, showing that the wave packet climbs up the vibrational ladder in PEC V_{11}^d in the first period ($0 < t < 20\,000$ a.u.), followed by a sequence of quick transitions (spikes) to PEC V_{22}^d in the second period ($20\,000 < t < 60\,000$ a.u.), and finally progresses down the slope to reach the target in the last (third) period ($60\,000 < t < 80\,000$ a.u.). These rapid transitions (spikes) involve different vibrational levels on the two PECs. The expectation value of position $\langle s \rangle$, Fig. 9(b), depicts the vibrational motion in PEC V_{11}^d in the first half ($0 < t < 40\,000$ a.u.) and in PEC V_{22}^d in the second half ($40\,000 < t < 80\,000$ a.u.) of the control interval. Figure 9(c) shows that the population of PEC V_{11}^d , $\langle \psi_1 | \psi_1 \rangle$, remains around 0.05 near the end of the control interval and the norm of the wave packet, $\langle \psi | \psi \rangle$, drops to about 0.7, indicating that a substantial portion of the population has dissociated. As suggested above, an intense control field may be required for pathway 2 to make a quick transition to PEC V_{22}^d in order to mitigate leakage of the wave packet into the asymptotic region. Snapshots of the wave-packet components for PECs V_{11}^d and V_{22}^d are shown in Fig. S4 in the supplementary material.⁴³

2. Cases 2–4

Table II also shows that the final optimal yields for cases 2–4. It was found that the results for cases 1 and 3 are about

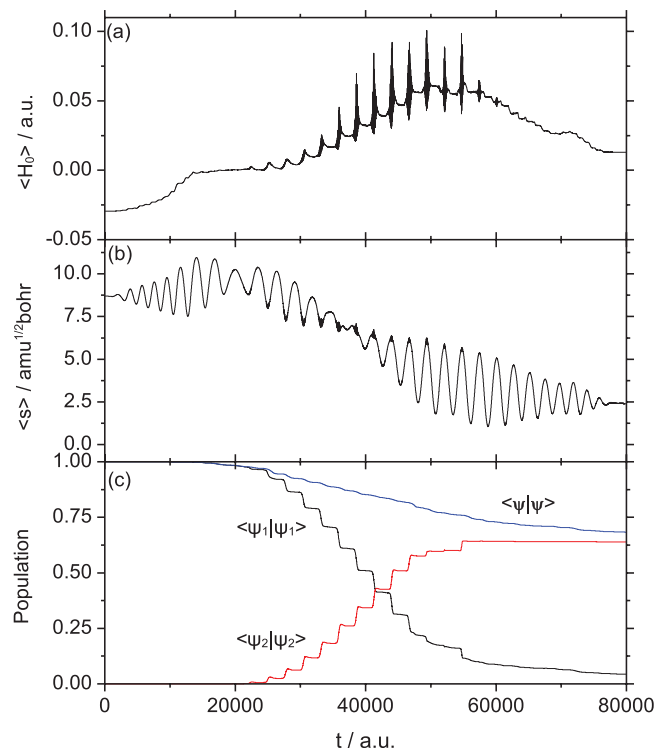


FIG. 9. Temporal changes driven by the optimal field for case 1 of pathway 2, given in Fig. 8(a): (a) the expectation value of the molecular field-free Hamiltonian, $\langle H_0 \rangle$. The origin of the vertical axis corresponds to the asymptotic energy of V_{11}^d ; (b) the expectation value of position, $\langle s \rangle$; (c) the populations of the diabatic states V_{11}^d and V_{22}^d and the norm of wave packets, $\langle \psi_1 | \psi_1 \rangle$, $\langle \psi_2 | \psi_2 \rangle$, and $\langle \psi | \psi \rangle$.

the same (here equal to 0.637 and 0.657, respectively) and so are those for cases 2 and 4 (0.531 and 0.540, respectively), despite having nearly the same field amplitudes and fluencies. These results indicate that the diabatic coupling may have a substantial effect on the final yield, while the TDM has a negligible effect around the AC point. Cases 2 and 4 show that a larger dipole coupling can more likely induce population oscillation between the two PECs V_{11}^d and V_{22}^d , thus generate more loss due to dissociation in PEC V_{11}^d . Nevertheless, despite the differences in the final yields, there is little difference in the temporal shapes and spectra of the optimal fields and in the behavior of $\langle H_0 \rangle$ and $\langle s \rangle$ for all four control scenarios, indicating very similar controlled dynamics.

C. Nonlinear field effects on pathway 2

In contrast to pathway 1, nonlinear field effects can drastically alter the control mechanism along pathway 2. Figure 10(a) shows that the optimal field deduced from including the nonlinear field effects due to polarizability and hyperpolarizability has large amplitudes between $t = 20\,000$ and $40\,000$ a.u. and becomes significantly negative around $t = 30\,000$ a.u. The optimal field has a broad frequency spectrum, as shown in Fig. 10(b). In particular, it contains strong, very low frequency components. The low frequency components around 0.005 a.u. (the inset of Fig. 10(b)) correspond to the vibrational level spacings of either PEC V_{11}^d or PEC V_{22}^d . Frequency components of small amplitude are widely distributed

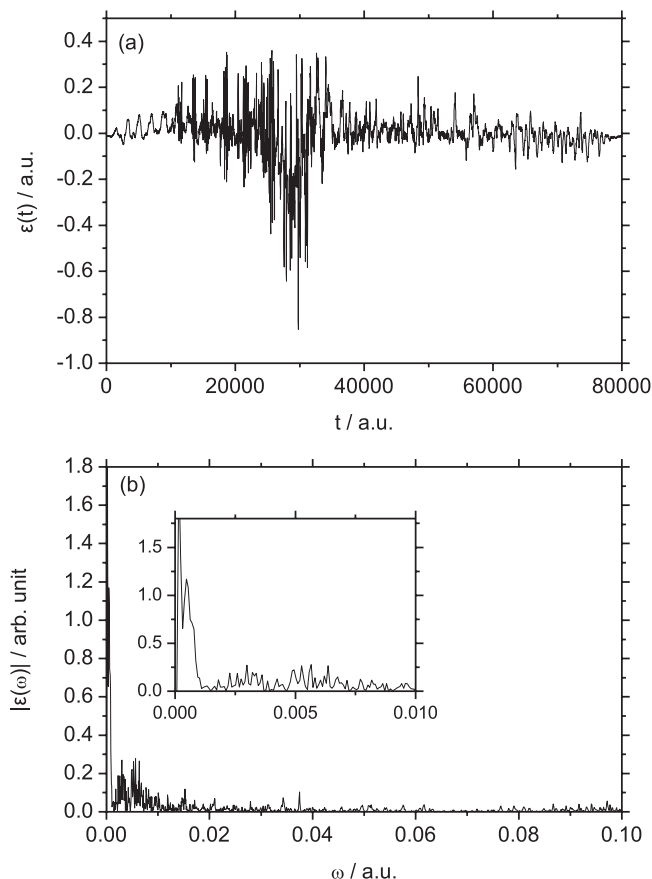


FIG. 10. (a) The optimal field and (b) its spectrum for case 1 of pathway 2, obtained when considering nonlinear field effects.

over the range 0.02–0.1 a.u., suggesting that the electronic transition from PEC V_{11}^d to PEC V_{22}^d occurs at many transition energies. In the supplementary material⁴³ we give the relevant figures: Husimi plot of the optimal field (Fig. S7); $\langle H_0 \rangle$, $\langle s \rangle$, $\langle \psi_1 | \psi_1 \rangle$, $\langle \psi_2 | \psi_2 \rangle$, and $\langle \psi | \psi \rangle$ (Fig. S8); snapshots of the wave-packet components for PECs V_{11}^d and V_{22}^d (Fig. S5). As summarized in Table II, the final yield with this field is 0.858 and the maximum field amplitude and fluence are 0.855 and 607.1 a.u., respectively. The final yield is substantially larger when compared to the case neglecting the nonlinear field effects.

The nonlinear field effects induced by strong low-frequency components in the resultant optimal control field between $t = 15\,000$ a.u. and $t = 40\,000$ a.u. (Fig. 10) appear to enable a quick electronic transition from PEC V_{11}^d to PEC V_{22}^d to avoid leakage of the wave packet into the asymptotic region (Fig. S5). A large Stark effect can arise as a result of these strong field components and, thus, modulate the two electronic PECs, thereby allowing for additional transitions. Moreover, the inclusion of nonlinear terms associated with polarizability and hyperpolarizability may further induce multiphoton electronic transitions that were not accounted for in the optimal control simulations without these nonlinear terms. In the simulation for pathway 2 including the nonlinear field effects resulted in a significantly higher final yield (Table II).

VI. SUMMARY

A two-state diabatic 1D reaction-path model has been constructed from the lowest five $^1A'$ PECs obtained from high-level *ab initio* calculations for ozone open \rightarrow cyclic isomerization optimal control simulations. Two possible pathways (Fig. 2(b)) were identified along with the associated band-limited control fields. Specifically, we performed four OCT calculations using various combinations of diabatic couplings and TDMs for both pathways around the AC point. The OCT calculations for pathway 1 from all four cases revealed similar outcomes, regardless of whether the nonlinear effects are considered. The OCT results for pathway 2 from all four cases showed that the strength of the diabatic coupling can significantly affect the final yields. It was also found that due to large amplitude of the resultant optimal control fields the nonlinear field effects notably change the control mechanism for pathway 2 and can enhance the final yield. The results show that pathway 1 is much more efficient, thus suffering much less photodissociation loss than pathway 2.

Pathway 2 in the current two-state model is similar to that undertaken in the single-state 1D model in our previous study,³³ with both being directly competing with the dissociation asymptote. In contrast, the optimal fields for pathway 1 exploit a secondary shallow well in the excited electronic state to bypass the dissociation channel, and as a result, producing higher final target state yields. As shown in Fig. 1, the excited 1D PECs are quite complex and there are likely some PEC regions, including the shallow well on PEC V_{22}^d , that can relay the wave packet to the target with high efficiency. The study suggests that the ozone isomerization control dynamics is greatly enhanced by appropriate band-limited electric fields with the aid of excited PECs.

ACKNOWLEDGMENTS

This work was supported in part by the Japan Society for the Promotion of Science (JSPS) KAKENHI Grant No. 20360423. The computations were performed using the supercomputers at Center for Computational Science & e-Systems, JAEA, Tokai, Ibaraki, Japan and also at Research Center for Computational Science, Okazaki, Aichi, Japan. T.-S. Ho and H. Rabitz acknowledge support by the U.S. Department of Energy under Grant No. DE-FG02-02ER15344.

¹S. A. Rice and M. Zhao, *Optical Control of Molecular Dynamics* (Wiley, New York, 2000).

²V. S. Letokhov, *Laser Control of Atoms and Molecules* (Oxford University Press, New York, 2007).

³M. Shapiro and P. Brumer, *Quantum Control of Molecular Processes* (Wiley-VCH, Weinheim, 2012).

⁴L. Pauling, *The Nature of the Chemical Bond* (Cornell Univ. Press, Ithaca, 1960).

⁵S. D. Peyerimhoff and R. J. Buenker, *J. Chem. Phys.* **47**, 1953 (1967).

⁶S. Shih, R. J. Buenker, and S. D. Peyerimhoff, *Chem. Phys. Lett.* **28**, 463 (1974).

⁷A. Banichevich, S. D. Peyerimhoff, and F. Grein, *Chem. Phys. Lett.* **173**, 1 (1990).

⁸A. Banichevich and S. D. Peyerimhoff, *Chem. Phys.* **174**, 93 (1993).

⁹P. J. Hay, T. H. Dunning, Jr., and W. A. Goddard III, *Chem. Phys. Lett.* **23**, 457 (1973).

¹⁰P. J. Hay and T. H. Dunning, Jr., *J. Chem. Phys.* **67**, 2290 (1977).

¹¹P. G. Burton and M. D. Harvey, *Nature (London)* **266**, 826 (1977).

¹²P. G. Burton, *J. Chem. Phys.* **71**, 961 (1979).

¹³J. S. Wright, *Can. J. Chem.* **51**, 139 (1973).

¹⁴G. Karlström, S. Engström, and B. Jönsson, *Chem. Phys. Lett.* **57**, 390 (1978).

¹⁵R. O. Jones, *J. Chem. Phys.* **82**, 325 (1985).

¹⁶T. J. Lee, *Chem. Phys. Lett.* **169**, 529 (1990).

¹⁷A. S. Shalabi, *J. Mol. Struct.: THEOCHEM* **262**, 131 (1992).

¹⁸S. S. Xantheas, G. J. Atchity, S. T. Elbert, and K. Ruedenberg, *J. Chem. Phys.* **94**, 8054 (1991).

¹⁹G. J. Atchity and K. Ruedenberg, *Theor. Chem. Acc.* **96**, 176 (1997).

²⁰T. Muller, S. S. Xantheas, H. Dachsel, R. J. Harrison, J. Nieplocha, R. Shepard, G. S. Kedziora, and H. Lischka, *Chem. Phys. Lett.* **293**, 72 (1998).

²¹R. Siebert, P. Fleurat-Lessard, R. Schinke, M. Bittererová, and S. C. Farantos, *J. Chem. Phys.* **116**, 9749 (2002).

²²R. Siebert and R. Schinke, *J. Chem. Phys.* **119**, 3092 (2003).

²³Z.-W. Qu, H. Zhu, and R. Schinke, *J. Chem. Phys.* **123**, 204324 (2005).

²⁴R. Schinke and G. C. McBane, *J. Chem. Phys.* **132**, 044305 (2010).

²⁵D. Xenides and G. Maroulis, *J. Phys. B: At. Mol. Opt. Phys.* **31**, L951 (1998).

²⁶G. Maroulis, *J. Chem. Phys.* **111**, 6846 (1999).

²⁷A. Haskopoulos and G. Maroulis, *Chem. Phys. Lett.* **397**, 253 (2004).

²⁸R. Elliott, R. Compton, R. Levis, and S. Matsika, *J. Phys. Chem. A* **109**, 11304 (2005).

²⁹L. De Vico, L. Pegado, J. Heimdal, P. Söderhjelm, and B. O. Roos, *Chem. Phys. Lett.* **461**, 136 (2008).

³⁰A. Kalemou and A. Mavridis, *J. Chem. Phys.* **129**, 054312 (2008).

³¹J.-L. Chen and W.-P. Hu, *J. Am. Chem. Soc.* **133**, 16045 (2011).

³²M. Artamonov, T.-S. Ho, and H. Rabitz, *Chem. Phys.* **305**, 213 (2004).

³³Y. Kurosaki, M. Artamonov, T.-S. Ho, and H. Rabitz, *J. Chem. Phys.* **131**, 044306 (2009).

³⁴B. Flemmig, P. T. Wolczanski, and R. Hoffmann, *J. Am. Chem. Soc.* **127**, 1278 (2005).

³⁵R. Plass, K. Egan, C. Collazo-Davila, D. Grozea, E. Landree, L. D. Marks, and M. Gajdardziska-Josifovska, *Phys. Rev. Lett.* **81**, 4891 (1998).

³⁶K. Fukui, *Acc. Chem. Res.* **14**, 363 (1981).

³⁷T.-S. Ho, H. Rabitz, F. J. Aoiz, L. Bañares, S. A. Vázquez, and L. B. Harding, *J. Chem. Phys.* **119**, 3063 (2003).

³⁸H.-J. Werner, P. J. Knowles, R. Lindh, F. R. Manby, M. Schütz *et al.*, MOLPRO, version 2006.1, a package of *ab initio* programs, 2006, see <http://www.molpro.net>.

³⁹H.-J. Werner and P. J. Knowles, *J. Chem. Phys.* **89**, 5803 (1988).

⁴⁰P. J. Knowles and H.-J. Werner, *Chem. Phys. Lett.* **145**, 514 (1988).

⁴¹T. H. Dunning, *J. Chem. Phys.* **90**, 1007 (1989).

⁴²R. Schinke, *Photodissociation Dynamics* (Cambridge University Press, Cambridge, 1993).

⁴³See the supplementary material at <http://dx.doi.org/10.1063/1.4865813> for the constructions of diabatic two-state 1D models for potential energy, dipole moment, polarizability, and hyperpolarizability. The detailed values of these quantities along the IRC are also tabulated and plotted.

⁴⁴C. C. Marston and G. G. Balint-Kurti, *J. Chem. Phys.* **91**, 3571 (1989).

⁴⁵S. Shi and H. Rabitz, *J. Chem. Phys.* **92**, 364 (1990).

⁴⁶W. Zhu, J. Botina, and H. Rabitz, *J. Chem. Phys.* **108**, 1953 (1998).

⁴⁷K. Sundermann and R. de Vivie-Riedle, *J. Chem. Phys.* **110**, 1896 (1999).

⁴⁸*Digital Signal Processing*, IEEE Press Selected Reprint Series edited by L. R. Rabiner and C. M. Rader (IEEE Press, New York, 1972).

⁴⁹D. G. Truhlar and B. C. Garrett, *J. Phys. Chem. A* **107**, 4006 (2003).

⁵⁰M. D. Feit and J. A. Fleck, Jr., *J. Chem. Phys.* **78**, 301 (1983).

⁵¹M. D. Feit and J. A. Fleck, Jr., *J. Chem. Phys.* **80**, 2578 (1984).

⁵²J. Broeckhove, B. Feyen, L. Lathouwers, F. Arickx, and P. Van Leuven, *Chem. Phys. Lett.* **174**, 504 (1990).

⁵³N. Balakrishnan, B. D. Ersy, H. R. Sadeghpour, S. T. Cornett, and M. J. Cavagnero, *Phys. Rev. A* **60**, 1407 (1999).

⁵⁴S. Mahapatra and N. Sathyamurthy, *J. Chem. Soc., Faraday Trans.* **93**, 773 (1997).